Four-dimensional visualization of single and multiple laser filaments using in-line holographic microscopy

Daryoush Abdollahpour,[1,2,*] Dimitrios G. Papazoglou,[1,3] and Stelios Tzortzakis[1,3,†]

[1]*Institute of Electronic Structure and Laser, Foundation for Research and Technology Hellas, P.O. Box 1527, GR-71110 Heraklion, Greece*

[2]*Physics Department, University of Crete, GR-71003 Heraklion, Greece*

[3]*Materials Science and Technology Department, University of Crete, GR-71003 Heraklion, Greece*

(Received 6 June 2011; published 4 November 2011)

It is shown, both through simulations and experiments, that the in-line holographic microscopy technique can be used to retrieve very small refractive-index perturbations caused during the filamentation of ultrashort laser pulses. This technique provides the possibility of having spatially and temporally (four dimensions) resolved measurements of refractive-index changes, down to 10^{-4}, from objects with diameters as small as 10 μm. Moreover, we demonstrate the power of the technique in discriminating multiple filaments in a precise quantitative way.

DOI: 10.1103/PhysRevA.84.053809 PACS number(s): 42.30.−d, 42.65.Re, 42.65.Jx, 42.25.Bs

I. INTRODUCTION

Filamentation of ultrashort laser pulses is a subject of significant interest in contemporary strong-field physics. The still increasing attention to this physical phenomenon is due to the fact that filamentation is a result of complex nonlinear optical phenomena that are promising for different applications and open new frontiers in different domains of physics. Although different physical mechanisms have been proposed to describe the filamentary propagation of ultrashort laser pulses, in a simplified view, filamentation can be considered as a dynamical balance between Kerr self-focusing and plasma defocusing, together with some other linear and nonlinear effects such as diffraction, nonlinear losses, etc. [1]. When the optical power in a pulsed beam exceeds the critical power of self-focusing, $P_{cr} \approx \lambda_0^2/8n_0n_2$($\lambda_0$, n_0, and n_2 are the central wavelength of the optical pulse, the refractive index, and the nonlinear refractive index of the medium, respectively), the optical beam tends to focus (for materials with $n_2 > 0$) and due to the high intensities reached near the focus, photoionization starts up, through tunnel, multiphoton, and avalanche ionization, depending on the optical pulse duration and the medium [1]. Ionization results in an underdense plasma that defocuses the beam. If the remaining laser power is still above the critical power, Kerr self-focusing takes over and the cycle is repeated again and again. This procedure leads to the filamentary propagation of ultrashort laser pulses with an almost constant narrow waist (a few μm to about 100 μm, depending on the medium) over propagation distances much longer than the Rayleigh range (filamentation over hundreds of meters in atmosphere has been reported [2,3]). Furthermore, if the input laser power is much higher than the critical one ($>10P_{cr}$), modulation instability will result in the appearance of multiple filaments [4].

Filamentation is followed by a number of characteristic attributes such as spectral broadening (which leads to pulse shortening or splitting), conical emission and supercontinuum generation, emission of electromagnetic waves in a wide range from UV to rf and THz, generation of a narrow, low-density conducting plasma string, etc. Owing to these properties filaments have found numerous applications in different fields such as triggering and guiding lightning and electrical discharges [5–7], Light detection and ranging (LIDAR) [8,9], remote laser-induced breakdown spectroscopy [10–12], micromachning, nanomachining [13–15], creation of plasma photonic devices [16], etc. Finally, for many applications optimization and tailoring of the filament properties is needed [17].

In any case, laser-generated plasma plays an important role in the formation of light filaments, their properties, and their applications. Thus characterizing the attributes of the filamentation-induced plasma strings is of great importance for understanding the fundamentals of filamentation and the accompanying physical effects, manipulation, and control of the propagation, and optimization and efficient design of the applications.

Due to the very high intensities ($10^{13}-10^{14}$W cm^{-2}) in the optical filaments, no physical probe can be placed directly in the propagation path, as it will be permanently damaged. Different techniques have been used to characterize the filamentary propagation and plasma string formation and its attributes. Among the most widely used techniques are plasma conductivity measurement [18–21], interferometry [22,23], diffractometry, shadowgraphy [19,24,25], and holographic techniques [26–30].

The plasma conductivity technique can be used to measure the filamentary propagation range by measuring the temporally averaged relative electron density in a plasma string. Although this technique is not very complicated for practical use, it has a number of drawbacks. One of the main drawbacks of this technique is the lack of resolution; spatial resolution of this technique is determined by the dimensions and geometry of the electrodes. Furthermore, because of the applied high voltages, this technique is not applicable for studying filamentation in solids. On the other hand, interferometry, diffractometry, and holographic techniques can be used for time-resolved measurements. However, because of the very small refractive-index changes induced by the plasma ($\Delta n \sim 10^{-3}$) as well as the small thickness of plasma strings (a few μm to $\sim$100 μm),

*Corresponding author: dabdolah@iesl.forth.gr

†stzortz@iesl.forth.gr

the accumulated phase change on a traversing probe beam can be in the order of a few mrad. Therefore, interferometric techniques are commonly used in the laser-plasma interactions with electron densities higher than 10^{17} cm^{-3}. Moreover, techniques like diffractometry and shadowgraphy, which use a single intensity profile to reconstruct the amplitude and the phase of the perturbed probe wave front, have serious limitations due to the emergence of an artifact well known in holography as twin image [31,32]. This artifact deteriorates the quality of the reconstructed wave front and can lead to ambiguous results. Its deteriorating action is more profound when studying plasmas in solids, where both the real and the imaginary parts of the refractive index are perturbed, and in dense plasmas in gasses. In an abstract mathematical approach, the twin image problem arises from the fact that one measures only the amplitude of the diffracted probe wave and not its phase, so the inverse problem is ambiguously posed.

In order to adequately address the above-mentioned problems, we have recently developed an accurate and powerful pump-probe in-line holographic microscopy (i-HOM) technique [29]. This technique is capable of measuring small transient changes (down to $\sim 10^{-4}$) in both the imaginary and real part of the refractive index of microsized volumes. It is based on the use of a bitelecentric microscope system that allows the accurate capturing of in-line holographic images of the perturbed probe beam. The amplitude and phase of the perturbed probe beam are then accurately retrieved by an iterative wave-front propagation algorithm. The three-dimensional distribution of the real and the imaginary parts of the refractive-index perturbation are then revealed using Abel inversion.

In this paper, the i-HOM technique is comprehensively studied, including a detailed theoretical and experimental analysis. We show, using both experiments and simulations, that i-HOM is a very sensitive technique that combines high spatial and temporal resolution and is capable of retrieving the micrometric refractive-index variations in four dimensions (x, y, z, and t). In Sec. II, after introducing the theoretical principles of the technique, the iterative process of the original wave-front reconstruction is described giving examples for different simulated objects. In Sec. III, experimental details of the technique are explained and the experimental results of studying a single filament in air are investigated. Furthermore, in this section, the role of the number of input in-line holograms on the convergence efficiency of the reconstruction algorithm is discussed. In Sec. IV, the potential of the technique to study multiple filaments is studied both numerically and experimentally by investigation of a double filamentary structure with different spatial arrangements.

II. PRINCIPLES OF IN-LINE HOLOGRAPHIC MICROSCOPY

The aim of the i-HOM technique is to accurately retrieve the amplitude and phase changes imprinted on the wave front of a probe beam after interaction with a pump-affected area. As mentioned in the Introduction, due to the high intensity of the pump beam, several nonlinear phenomena take place in the focal area, including the optical Kerr effect, multiphoton absorption, ionization, and plasma generation.

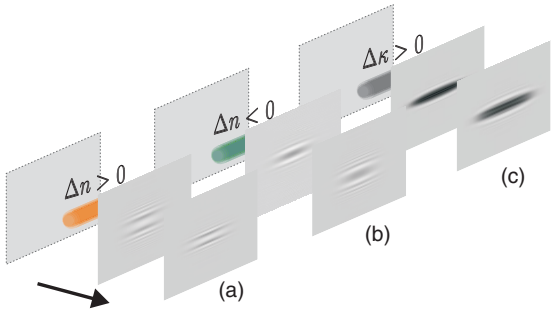

FIG. 1. (Color online) Typical holographic diffraction images for a probe perturbed by a cylindrical structure with (a) $\Delta n > 0$ ($\Delta\kappa = 0$), (b) $\Delta n < 0$ ($\Delta\kappa = 0$), and (c) $\Delta\kappa \neq 0$ ($\Delta n = 0$).

In general, these effects lead to the perturbation of the refractive index $\Delta\tilde{n} = \Delta n + i\,\Delta\kappa$, in the real ($\Delta n$) and/or in the imaginary part ($\Delta\kappa$). Thus, as the probe wave front propagates through the pump-affected area, the transient changes in the refractive index act as diffracting structures. Figure 1 shows typical holographic diffraction images (simulated) of a propagating plane probe wave front after interaction with a refractive (or absorbing) cylindrical structure. It is clear that in all cases the amplitude of the probe wave is affected by the presence of the structure and that the wave front is evolving as it propagates. The phase of the probe wave front follows a similar behavior so that after a short propagation distance the probe wave is perturbed both in amplitude and phase even in cases where only the real or only the imaginary part of the refractive index are perturbed. This complex evolution of the perturbed probe wave front is a well-known effect of the Fresnel diffraction process and can be exploited to retrieve both its amplitude and phase only from intensity measurements.

A very effective way of analyzing the propagation of wave fronts is the concept of the angular spectrum [29,32]. The various Fourier components of the complex light field $U(x,y;z)$ can be identified as a sum of plane waves traveling in different directions, i.e., different **k** vectors often referred to as angular spectrum. Thus, the field distribution at any other plane can be calculated by adding the contribution of these plane waves taking into account the phase shift they acquire during the propagation up to that point. Therefore, the complex light field at any point can be written as [29]

$$U(x,y;z) = \iint P_{z_0}(l_x,l_y)e^{i2\pi(z-z_0)\sqrt{1-l_x^2-l_y^2}}e^{i2\pi(xl_x+yl_y)} \times dl_x\,dl_y, \tag{1}$$

where x, y, z are the spatial coordinates measured in the probe beam wavelength units (λ), l_x,l_y are the direction cosines of each plane wave, and $P_{z_0}(l_x,l_y)$ is the angular spectrum of the complex field distribution at $z = z_0$, and it is given by

$$P_{z_0}(l_x,l_y) = \iint U(x,y;z_0)e^{-i2\pi(l_x x+l_y y)}dx\,dy, \tag{2}$$

which is a two-dimensional Fourier transformation of the complex light field distribution at $z = z_0$. If both the amplitude and the phase distributions of the light field at a specific position along the propagation are known, the complex light field at any other propagation distance can be numerically calculated by using Eq. (1). Unfortunately, optical detectors

such as charge-coupled device (CCD) cameras are capable of recording only the intensity, and thus the amplitude of the light field. The unknown phase, although not directly measurable, drastically affects the intensity of the light field as the wave propagates. This intensity variation can then be used to retrieve the unknown phase of the wave front. Therefore, instead of using a single holographic diffraction image one could combine several holographic diffraction images along the wave propagation in order to be able to retrieve the phase along with the amplitude [29,33].

More specifically, a CCD camera located at a plane position z, records the intensity distribution $I(x,y;z)$ and thus the amplitude $|U(x,y;z)| = \sqrt{I(x,y;z)}$ of the diffracted light field. The recorded diffracted light field intensity $I(x,y;z)$ is actually an in-line Gabor hologram [34]. Although one can numerically back propagate a plane wave through this hologram the original wave front cannot, in general, be retrieved due to the appearance of a conjugate twin image [32]. This twin image appears in the wave-front reconstruction as an undesirable, conjugate replica of the original object positioned symmetrically to the hologram. As we have already discussed, it originates from the fact that only the amplitude of the propagating wave front is measured. We follow an iterative approach [29,33] in order to overcome this problem and determine both the phase and amplitude of the diffracted light field. A graphical representation of this approach is depicted in Fig. 2.

We start by recording a series of in-line holograms $I(x,y;z_i)$, at several positions z_i $(i = 1,2,\ldots,N)$ along the propagation direction. Starting from a plane at position z_1, the light field is set as $U(x,y;z_1) = \sqrt{I(x,y;z_1)}\exp[i\varphi_{1,1}(x,y)]$, where $I(x,y;z_1)$ is the recorded intensity pattern (in-line hologram) at the plane located at z_1 and $\varphi_{1,1}(x,y)$ is the initial seed phase distribution (the first subscript stands for the iteration number, while the second one indicates the plane number).

The initial phase distribution can be simply set to a constant value (plane wave) [29] or, to accelerate the convergence

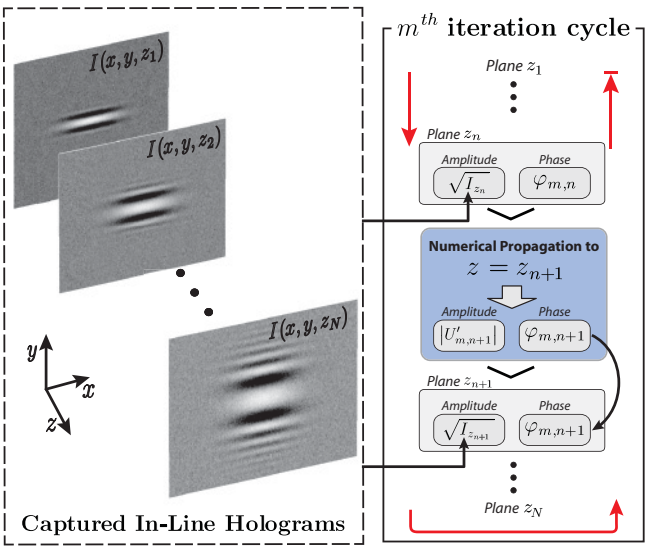

FIG. 2. (Color online) Schematic representation of the wave-front retrieval algorithm (see text).

of the iterative process, to a distribution closer to the final one such as the one predicted from the holographic reconstruction of the retrieved in-line holograms. By using Eqs. (1) and (2), the complex light field $U'_{1,2}(x,y;z_2)$ at the second plane located at z_2 is numerically estimated. At this point, by combining the experimentally measured intensity $I(x,y;z_2)$ with the numerically estimated phase $\varphi_{1,2}(x,y) = \arg[U'_{1,2}(x,y;z_2)]$, we set a new estimation of the complex light field $U_{1,2}(x,y;z_2) = \sqrt{I(x,y;z_2)}\exp[i\varphi_{1,2}(x,y)]$. We repeat this numerical procedure up to the last plane at position z_N and then we back propagate toward the first plane at position z_1, and this completes the first iteration cycle. The iterations are repeated M times until the calculated complex amplitude $U'_{M,i}(x,y;z_i)$ can adequately predict the experimentally measured intensity $I(x,y;z_i)$. The level of convergence is determined by the merit function:

$$C_m = \sum_{i=1}^{N} \frac{\int\int[|U'_{m,i}(x,y;z_i)| - \sqrt{I(x,y;z_i)}]^2 dx\,dy}{\int\int I(x,y;z_i)dx\,dy}. \quad (3)$$

To explore the capabilities of the wave-front retrieval iterative algorithm, we have first tested its accuracy on simulated sets of in-line holograms. To facilitate the computational effort in these numerical experiments the sets are composed of one-dimensional wave fronts. This wave-front distortion corresponds to the perturbation that would be induced on a plane wave by the presence of a purely refractive object with refractive-index distribution $n = n_0 + \Delta n\,\exp[-4(\ln 2)(y/d)^2]$, where n_0 is the refractive index of the surrounding medium, Δn is the refractive-index modulation ($\Delta n = -1.5 \times 10^{-2}$), and d is the diameter of the object at full width at half maximum (FWHM) ($d = 10\ \mu$m). The values are chosen so that they correspond to a typical situation of a laser-generated plasma string in air. In order to create the input in-line holograms of the iterative retrieval algorithm, the distorted wave front was numerically calculated at six propagation distances $z_{1-6} = 0$, 0.1, 0.2, 0.4, 0.8, and 2 mm and fed into the algorithm. Input in-line holograms are shown in Fig. 3(a). Simulated and retrieved amplitude and phase changes at $z = 0$ and $z = 2$ mm are shown in Figs. 3(b)–3(e). The loose constraint [$C = 10^{-3}$, Eq. (3)], for this simulation was reached after ~310 iterations. It is seen that the retrieved wave front perfectly matches the simulated ones. This is a clear demonstration of the ability of this iterative approach to accurately retrieve the phase distribution of an unknown wave front. Furthermore, for comparison purposes, the phase change corresponding to the same simulated object, retrieved by single-plane diffractometry, using only one diffraction pattern at $z = 2$ mm, is shown in Fig. 3(f); it is obvious that in this case, the retrieved wave front is significantly distorted due to the twin-image problem.

As a second step, we studied the robustness of the phase retrieval algorithm under the effect of noise. This is a typical situation in real experimental images where background noise cannot be entirely diminished. In this case we followed a similar numerical approach as the former situation ($\Delta n = -1.5 \times 10^{-2}$ and $d = 10\ \mu$m) but now in the presence of noise in the in-line holograms. The noise was implemented as a random variation of the calculated in-line hologram amplitude. The noise level was ~2%, comparable to the levels usually

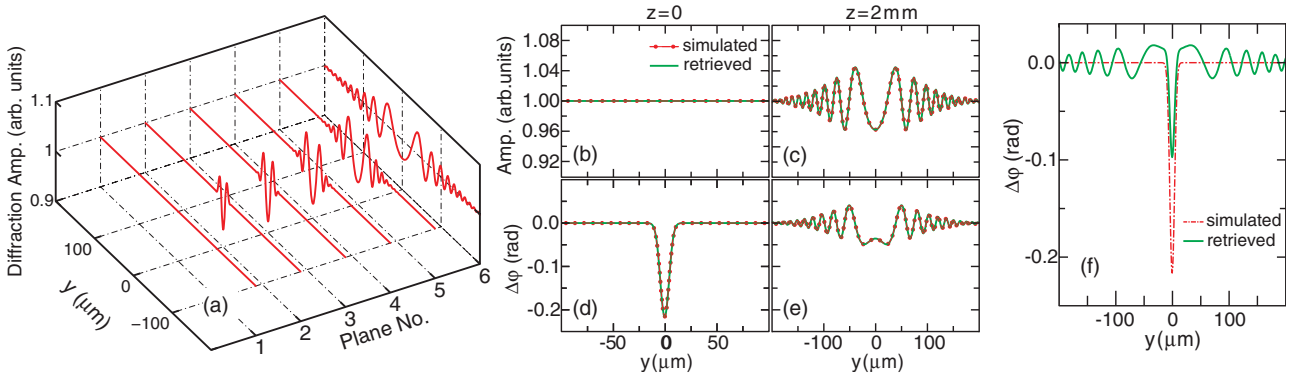

FIG. 3. (Color online) (a) Simulated input amplitude distributions (in-line holograms) corresponding to the phase object shown in (b) and (d); [(b)–(e)] simulated (initial) and retrieved phase and amplitude distributions by using i-HOM technique at two different propagation distances, $z = 0$ and $z = 2$ mm. (f) Simulated (initial) and retrieved phase change by using only one diffraction pattern at $z = 2$ mm.

encountered in experimental images. Figure 4(a) shows the simulated in-line holograms at different propagation distances $z_{1-6} = 0, 0.1, 0.2, 0.4, 0.8$, and 2 mm. We have to note here that as in a typical experiment, the noise amplitude does not depend on the propagation distance and thus the signal-to-noise ratio varies along the propagation. In our simulations, since the diffraction amplitude (signal) is very small on the first plane, the signal-to-noise ratio is close to zero, while for the other planes this ratio varies from minimum (∼6.5) on the second plane, to maximum (∼8.8) on the fourth plane.

The simulated and retrieved amplitude and phase distributions are shown in Figs. 4(b)–4(e). It is clear that the iterative algorithm is still capable of accurately retrieving the amplitude and phase of the wave front. The process though was now more computationally demanding since convergence was reached after ∼475 iterations. This effect is more profound at lower values of signal-to-noise ratios where convergence is reached after a higher number of iterations. Furthermore, the noise spectral distribution can affect the phase retrieval accuracy and required computational effort.

III. EXPERIMENTAL IMPLEMENTATION

As demonstrated in the previous section using, instead of one, a number of in-line holographic images, it is possible to accurately retrieve the phase distribution of a perturbed wave front. To implement this method experimentally one has to be able to capture in-line holograms along the propagation of the probe beam. The useful regime lies from just after the interaction area up to the lower boundary of the far-field Fraunhofer diffraction region since from thereon the wave front experiences a self-similar expansion with no variation in the intensity distribution. A useful quantitative criterion is the Fresnel number defined as $F \approx d^2/z$, where d is the diameter of the diffracting object and z is the propagation distance, both measured in wavelength units (λ). Under quite loose constraints we can assume that the lower boundary of the Fraunhofer diffraction region is at $F \cong 0.1$. Taking into account that typical sizes of diffracting objects under study (i.e., plasma strings) range from 10 to 100 μm, we find that the most useful measurement region is restricted to 0.8 and 80 mm. respectively (for $\lambda = 800$ nm). In-line holograms retrieved beyond this region can still be used in the iterative algorithm but in combination with in-line holograms recorded inside this region.

The first and most straightforward solution of the direct projection of the in-line holograms onto the sensor of a CCD camera has several restrictions. The working distance, defined by the useful range, depends on the size of the object under study, and sometimes is so small that it is very difficult

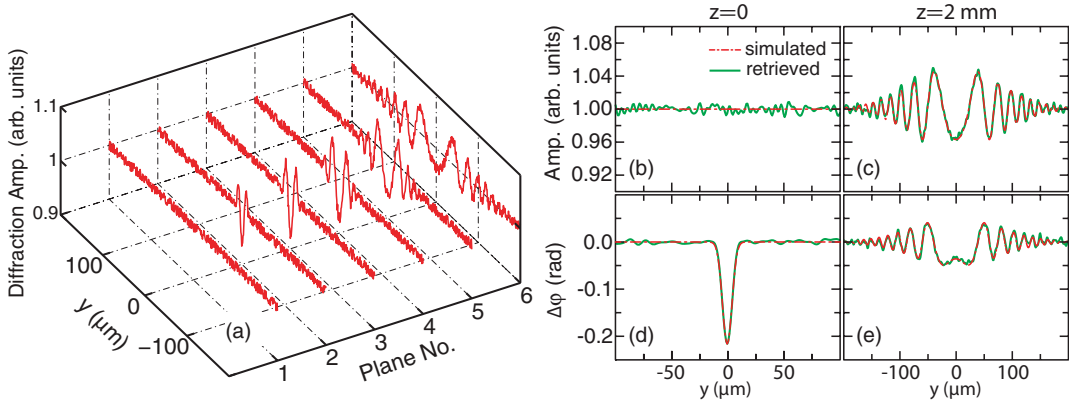

FIG. 4. (Color online) (a) Simulated amplitude distribution (in-line holograms) for various propagation distances with the addition of 2% random noise; [(b)–(e)] simulated and retrieved amplitude and phase distribution at two different propagation distances, $z = 0$ and $z = 2$ mm.

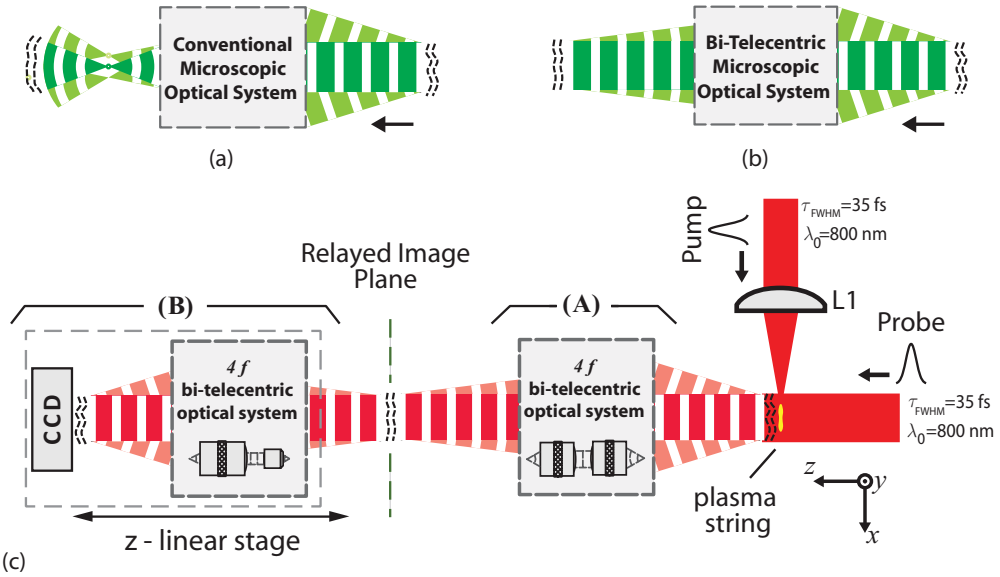

FIG. 5. (Color online) (a) Imaging in a typical microscope system. Plane waves are transformed to spherical ones. (b) Imaging using a bitelecentric optical system; plane waves are still plane after exiting the system. (c) Experimental setup of the pump-probe in-line holographic microscopy utilizing a cascade of bitelecentric optical systems.

to access if, for example, a bulk medium such as glass is studied. Furthermore, the typical CCD pixel size is in some cases comparable to the object size deteriorating the retrieval quality while the finite dimension of the CCD sensor sets a limit on the numerical aperture [26,29,33]. Furthermore, the sensor has to be displaced over a considerable distance along the z axis in order to acquire a sufficient number of holograms. To resolve these issues one has to remotely record the in-line holographic images. A typical microscope imaging system, although it overcomes the numerical aperture limitations, has some serious experimental complications. Using the concept of the angular spectrum, an imaging system will remotely access the holographic planes only if the angular spectrum is preserved during the imaging process. Thus, in order to preserve the angular spectrum, the imaging system should simply fulfill the following condition: a plane wave entering it should exit as a plane wave [29]. Unfortunately, in conventional optical microscope systems the angular spectrum is not preserved. As shown in Fig. 5(a), the plane waves $P_{z_0}(l_x,l_y)$ of the angular spectrum entering the microscope system are, in general, transformed to spherical waves in the image area so the angular spectrum is disturbed. In this case Eqs. (1) and (2) cannot be directly used to analyze and reconstruct the original wave front. In other words, the image remotely recorded on the CCD sensor will not be a scaled replica of the original in-line hologram. Likewise, the magnification in such an optical system depends on the position of the imaging plane. On the other hand, a bitelecentric optical system preserves the angular spectrum, as shown in Fig. 5(b), and thus the plane waves entering the system exit as plane waves. An optical system is bitelecentric when its entrance and exit pupils are located at infinity. Typically, any telescopic system (such as a 4f system) fulfills this condition. This results in an image that is a magnified replica of the original in-line hologram while the magnification factor is constant across the whole image zone.

We follow a bitelecentric microscopic method [29] to preserve the angular spectrum while overcoming all the above-mentioned limitations (numerical aperture, working distance, resolution, etc.). As shown in Fig. 5(c) the experimental setup is composed of a cascade of two 4f systems. The first one acts as a relaying system [part (A), Fig. 5(c)] and consists of a pair of high-quality photographic lenses. This first bitelecentric system provides a sufficiently long working distance (~50 mm). The second 4f system [part (B), Fig. 5(c)] is also bitelecentric and consists of a microscopic objective lens and a high-quality zoom photographic lens. The second subsystem can freely move along the z axis, while the magnification is independent of the propagation distance z. In this way, the angular spectrum is preserved and the outcome is a spatially magnified image of a conjugate plane in the object area. In this case, Eq. (1) can be rewritten as [29]

$$U(x,y;\Delta z) = \iint_{\mathrm{NA}} P_{z_o}(l_x,l_y) e^{i2\pi\Delta z\sqrt{1-l_x^2-l_y^2}} \times e^{i2\pi(l_x x+l_y y)} dl_x\, dl_y, \tag{4}$$

with

$$x = \frac{1}{M_{\mathrm{tot}}}x', \quad y = \frac{1}{M_{\mathrm{tot}}}y', \quad l_x = M_{\mathrm{tot}}l_x',$$
$$l_y = M_{\mathrm{tot}}l_y', \quad \Delta z = \frac{(z'-z_0')}{(M_1)^2},$$

where x,y,z are the spatial coordinates in the object region; x',y',z' are the spatial coordinates in the image region (CCD) measured in the probe beam wavelength (λ) units, l_x' and l_y' are direction cosines as they are transformed by the imaging system, NA refers to the numerical aperture of the optical system and practically limits the collected angular spectrum, M_{tot} is the total transverse magnification of the imaging system, and M_1 is the transverse magnification of the first 4f system. It can be clearly seen that Eq. (4) is very similar

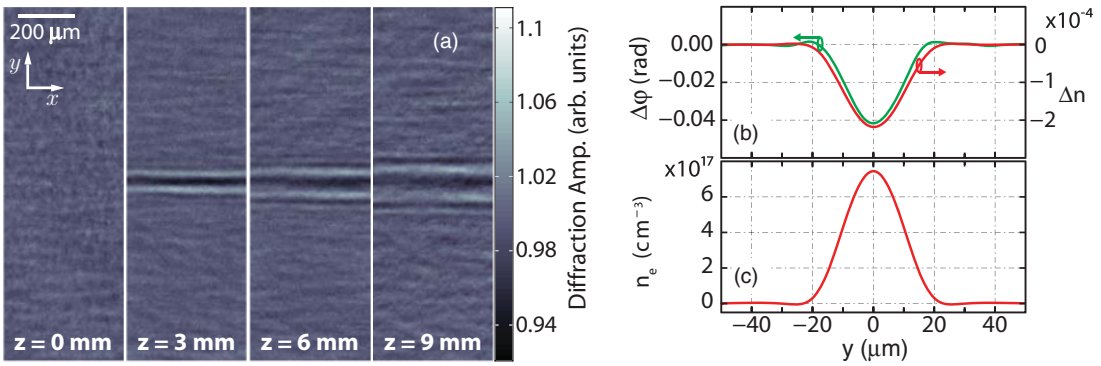

FIG. 6. (Color online) (a) Experimental in-line holograms remotely captured along the propagation of the probe beam, (b) retrieved phase and corresponding refractive-index change (Abel transform), and (c) respective electron-density distribution in the plasma string.

to Eq. (1) except that a displacement $\Delta z'$ is equivalent to a smaller displacement $\Delta z = \Delta z'/M_1^2$ in the object region. This can be beneficial from the experimental point of view since it provides a higher accuracy in determining the spacing between in-line holographic planes. In summary, this bitelecentric microscopic system provides the possibility of having wide view high-resolution images ($\sim$1.5 μm) of any holographic plane in the object area.

The experimental setup is composed of a standard pump-probe setup and the in-line holographic microscope system. The pulsed laser beam (35 fs at $\lambda = 800$ nm) is split in two arms in a pump-probe setup as shown in Fig. 5(c). The pump beam is focused by a converging lens (L1: $f = 300$ mm, 0.042 NA) and the collimated probe beam is traversing the focal region of the pump beam at 90°. The focal region (filamentation region) of the pump beam is imaged with the in-line holographic microscopic system. In this case, the total transverse magnification and the magnification of the subsystem A were $M_{\text{tot}} = 1.64$ and $M_1 = 1.42$, respectively. A linear CCD camera (12 bit, 1224 × 968 pixels) is used to remotely record the in-line holograms [part B, Fig. 5(c)]. The holograms at different planes are captured by moving the subsystem B in Fig. 5(c) along the z axis. The experimental system is fully computer automated in such a way that single-shot probe images can be recorded for various delays or for a finite number of accumulated pump laser pulses (of interest when studying propagation in transparent solids where accumulation effects can be important). The noise level in the captured in-line holograms is reduced by subtracting the beam-free background and pump-beam-induced emissions from the focal region, where filamentation occurs.

IV. EXPERIMENTAL RESULTS

In order to study the filamentation of ultrashort laser pulses, a pump beam with pulse energy $E_p = 0.45$ mJ, which corresponds to $P \simeq 3.9 P_{\text{cr}}$ (for $\lambda = 800$ nm, $P_{\text{cr}} = 3.3$ GW [4]), was focused using an $f = 300$ mm lens (0.042 NA) and created a single $\sim$1370-μm-long filament in air. The filament length was approximately nine times longer than the corresponding Rayleigh length (146 μm). Since the low-density plasma string has a long lifetime, a few hundreds of picoseconds [19], the delay between the pump and probe pulses was set at 6 ps, to have a net plasma contribution in the observed index changes. In-line holograms were recorded in four plane positions along the propagation direction of the probe beam, located at $z = 0$, 3, 6, and 9 mm. The position $z = 0$ corresponds to the location of the filament, as identified by imaging the corresponding low-intensity plasma emission. Typical images of remotely captured in-line holograms are shown in Fig. 6(a). Due to the elongated shape of plasma filaments in air, the diffraction pattern is practically uniform for considerable length along the pump propagation [x axis, Fig. 6(a)]. This enabled us to reduce the phase retrieval problem to one dimension by using averaged traces of the diffraction intensity over $\sim$420-μm-wide slices along the x axis. This of course is not a prerequisite for the iterative phase retrieval algorithm but simply dramatically reduces the computational effort and slightly increases the signal-to-noise ratio. In the general case that the diffraction pattern is not uniform, a full two-dimensional analysis has to be performed, as we will show below. The loose constraint for the iterative retrieval algorithm was set to $C = 10^{-3}$ [Eq. (3)], while convergence succeeded after $\sim$1000 iterations. The retrieved phase distribution of the perturbed probe beam is shown in Fig. 6(b) while the corresponding amplitude distribution (not shown) is flat. The refractive-index distribution, shown in Fig. 6(b), that caused this perturbation is recovered by using Abel inversion [29,35]. Likewise, the change in the refractive index can in turn be correlated to the plasma density distribution using a simple Drude model [1]. In this case, the free-electron density is analogous to the refractive-index distribution: $n_e = -2n_{\text{cr}}\Delta n$, where $n_{\text{cr}} = 1.7 \times 10^{21}$ cm^{-3} is the critical plasma density in air for an 800 nm probe beam. The corresponding electron-density distribution is shown in Fig. 6(c). These results are indicative of the power of the i-HOM technique. Through a series of diffraction images, the refractive-index distribution and the plasma density distribution of a $\sim$22-μm-wide plasma string in air with plasma density on the order of 10^{17} cm^{-3} is measured. The peak refractive-index change is as low as -2×10^{-4} and as is clearly visible from Fig. 6(b), the signal-to-noise ratio is very high.

We should note here that we do not observe any effect of the molecular alignment revivals (see, for instance, [36]) since the probe beam is transverse to the propagation of the pump. In this configuration, the effective interaction length between the probe beam and the filament is quite short (ranges from 10 to 50 μm). Thus, since the refractive-index perturbations

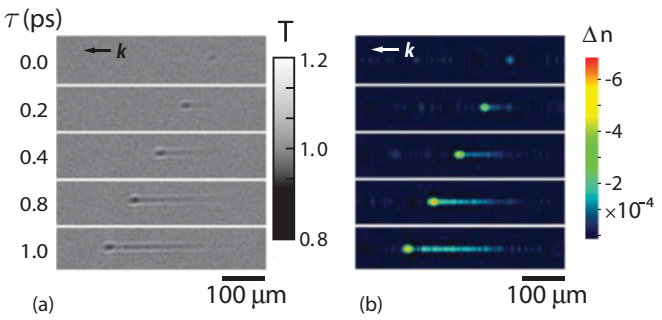

FIG. 7. (Color online) (a) Experimental in-line holograms of a propagating filament for various pump-probe delays (k is the pump wave vector). (b) Retrieved refractive-index distribution.

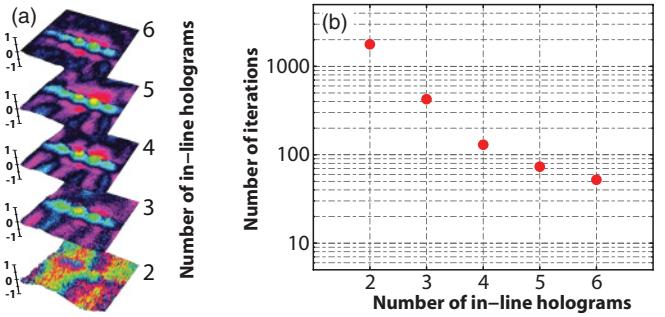

FIG. 8. (Color online) (a) Retrieved phase information as a function of the number of input in-line holograms. (b) Number of iterations to reach convergence (under the same constraint) versus the number of input in-line holograms.

associated to the molecular alignment are of the order of 10^{-6}, the corresponding phase change would be lower than $\sim$400 μrad, a value much smaller than our experimental phase resolution of a few mrad. Nevertheless, if one would like to study such small effects, the i-HOM technique can still be applied but with increased interaction length between the pump and the probe beams (by varying the crossing angle). Inevitably, in the latter case, there will be a compromise on the spatial resolution.

To clearly demonstrate the capability of the high-sensitivity and spatiotemporal resolution capabilities of the i-HOM technique, we also performed time-resolved experiments. In this case the pump beam with energy of 40 μJ, which corresponds to $P \cong 0.35\ P_{\rm cr}$, was focused in air using a lens with $f = 100$ mm (0.06 NA) and created a single $\sim$300-μm-long filament in air. The filament length was approximately four times longer than the corresponding Rayleigh length (71 μm). The remotely captured in-line holograms as a function of the probe delay are shown in Fig. 7(a). For each delay, six in-line holograms were captured and the phase and amplitude of the perturbed probe wave front were retrieved using the iterative retrieval algorithm. The corresponding distribution of the refractive-index perturbation is shown Fig. 7(b) and was retrieved by applying Abel inversion [29,35] to the wave-front phase. In the filament area the high intensity of the propagating pulse ignites multiphoton ionization and leads to the generation of plasma (peak plasma densities of 2.4×10^{18} cm^{-3} [29]) that lowers the refractive index. This refractive-index drop during the pump pulse as well as the remaining plasma trail is clearly distinguishable in Fig. 7(b). There one can also remark that the drop is faster at the end of the pulse, while in the following trail the decay is slower. This is an interesting phenomenon that could be related to the higher-order Kerr effect [37], or the enhanced electron plasma nonlinearity [38,39] present during the pump pulse. A detailed study on this effect, using other, shorter probe pulses, is presently under way and will be the subject of a future publication.

The efficiency and the computational load of the iterative reconstruction algorithm depend on the number of in-line holograms used. To study this, six in-line holograms of a typical short filament in air were recorded. Then, for a constant constraint, $C \leqslant 0.1$, the reconstruction algorithm performance was evaluated using different numbers of input in-line holograms. Figure 8(a) shows the retrieved phase ($-\Delta\varphi$) as a function of the number of input in-line holograms. It can be clearly seen that due to the effect of noise, the phase information can be barely retrieved with only two in-line holograms, but the effect of noise is significantly suppressed as we increase the number of in-line holograms. In Fig. 8(b), the number of iterations needed to reach the convergence (under the specified constraint) is shown as a function of the number of in-line holograms. Similarly, more input in-line holograms result in faster convergence of the algorithm.

V. INVESTIGATION OF MULTIPLE FILAMENTS USING IN-LINE HOLOGRAPHIC MICROSCOPY

So far, we have applied i-HOM to study single filaments; however, for higher laser pulse powers ($>10P_{\rm cr}$), multiple filamentation occurs. In this regime, modulational instabilities result in the generation of several light filaments and corresponding plasma strings with a random transverse distribution [4,40,41]. The stochastic behavior of multiple filamentation is not desirable for some applications wherein a precise localization or shot-to-shot stability of filaments is needed. Different approaches have been used to have a control on multiple filamentation. Of those methods, using an amplitude mask [42], introducing an ellipticity in the input beam [43], introducing a mesh into the beam [44], and applying high astigmatism by tilting the focusing lens [45] can be mentioned. In any case, characterization of organized multifilamentary structures can be useful for several applications as well as for optimization of multiple filamentation tailoring.

To examine the potential of i-HOM to characterize complex objects, we studied, using both simulations and experiments, double filamentary structures. In our simulations, two phase objects located on the same plane were representing the double filamentary structures with a refractive-index distribution given by

$$n = n_0 + \tfrac{1}{2}\Delta n[e^{-4\ln 2[(y-h/2)/d]^2} + e^{-4\ln 2[(y+h/2)/d]^2}], \qquad (5)$$

where n_0 is the refractive index of the surrounding medium, Δn is the refractive-index modulation ($\Delta n = -1 \times 10^{-3}$), h is the distance between two objects, and d is the diameter of each object [$d = 10$ μm (FWHM)]. Using these values we numerically propagated the known wave front at six propagation distances $z_{1-6} = 0$, 0.1, 0.2, 0.4, 0.8, and 1 mm and retrieved the corresponding phase and amplitude. The analysis

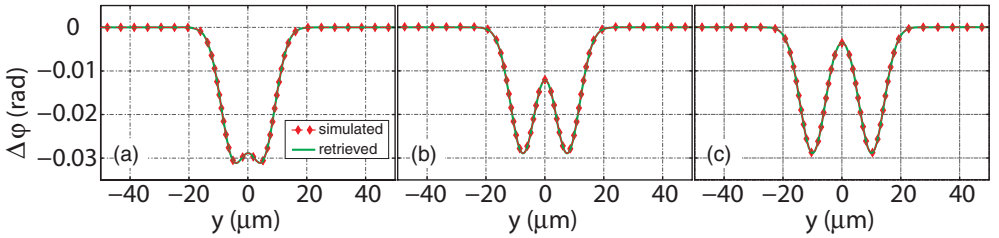

FIG. 9. (Color online) The simulated and retrieved phase change, corresponding to two refractive structures, located on the same plane along the z axis and separated by 10 (a), 15 (b), and 20 μm (c).

was repeated for several separation distances between the two phase objects: $h = 10$, 15, and 20 μm. The corresponding simulated and retrieved phase change distributions are shown in Figs. 9(a)–9(c), respectively.

It is clearly seen that the wave-front reconstruction algorithm is capable of distinguishing two different weak phase objects, no matter what the separation distance between them is. However, from the experimental point of view, distinguishing multiple filamentary structures is expected to have a limit because of the stochastic behavior of the multiple filamentation [4].

Experimentally, in order to create a double filamentary structure, the pump beam was split in two parts by using two joint mirrors mounted very close together. The total pump-beam energy was set to 1 mJ and this energy was approximately equally divided between two parts of the beam, so that each part of the beam would create only one filament. The split pump beam was focused with an $f = 300$ mm lens. By using this simple scheme, a double filamentary structure was created with the possibility of controlling the separation between them along both the z and the y axis. First, two filaments were adjusted to lie on the same z position, with different separations along the y axis. For each separation along y, in-line holograms were remotely captured at $z = 0$, 0.5, 1, 1.5, 2, and 2.5 mm and then fed into the original wave-front reconstruction algorithm. Typical in-line holograms corresponding to two separation distances of 145 and 72 μm between the filaments are shown in Figs. 10(a) and 10(b). Figures 10(c) and 10(d) show the corresponding retrieved phase distributions. The retrieved amplitude (not shown here) is flat, indicative again of the purely refractive nature of the diffracting object. The separation distance between the filaments as measured by the phase distribution profiles in Figs. 10(c) and 10(d) agree well with independent measurements of burn spot profiles on photographic paper placed perpendicularly to the propagation direction of the filaments and exposed to multiple laser shots.

Furthermore, as was expected, resolvability of two filaments is practically limited to a separation distance in which the filaments start to dynamically interact between them. The interaction between filaments results in chaotic distribution of plasma density, and therefore the intensity profile of the diffracted probe beam is not reproducible from shot to shot. In this case, recorded in-line holograms will be averaged out and the result of the reconstruction algorithm will not be accurate. For the present experimental condition, the minimum separation distance between filaments was ∼70 μm since below this distance the filaments start to interact.

Finally, we studied a more complicated three-dimensional arrangement by locating the double filamentary structures at two different planes. More specifically, in our experiment the two filaments were separated by ∼0.5 mm along the propagation direction of the probe beam. In-line holograms were captured at the same positions as in the previous experiment and were fed into the wave-front retrieval algorithm. To distinguish the two independent plasma strings the retrieved wave front was numerically propagated from $z = -4$ mm to $z = 4$ mm with a step size of 40 μm. The phase distribution as a function of the propagation distance is shown in Fig. 11(a). It

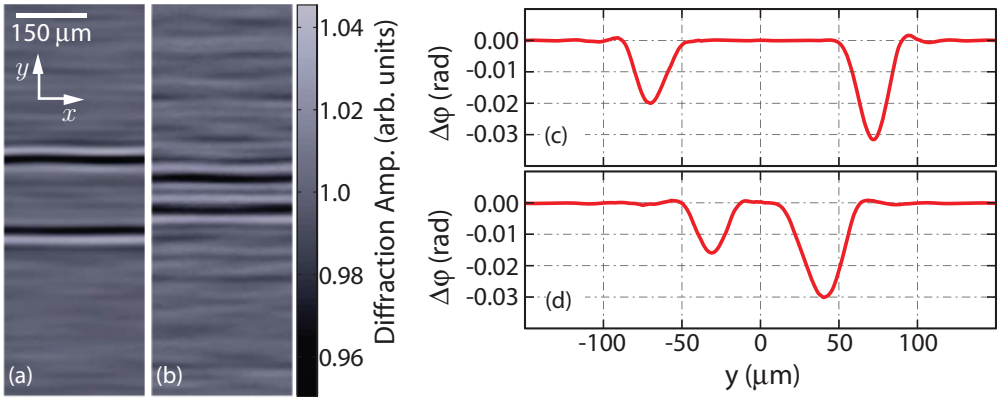

FIG. 10. (Color online) In-line holograms recorded at $z = 1.5$ mm, corresponding to two filaments located on the same plane along the propagation direction of the probe beam, z, separated by ∼145 μm (a) and ∼72 μm (b), along the y axis. [(c) and (d)] Retrieved phase change profiles corresponding to (a) and (b), respectively.

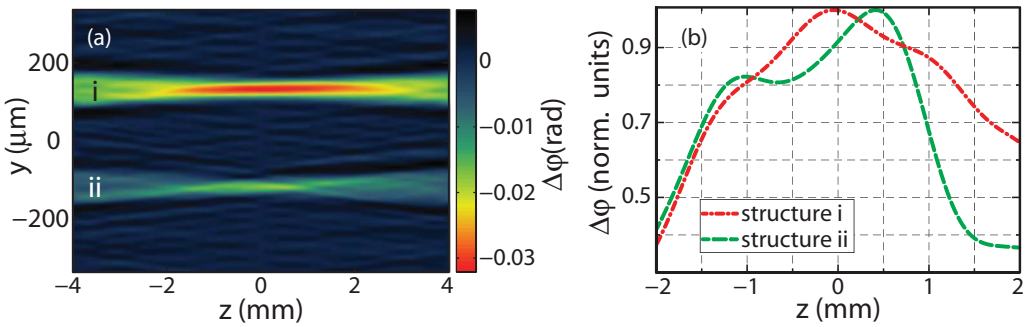

FIG. 11. (Color online) (a) Phase distribution of the numerically propagated wave front as a function of the propagation distance z and (b) normalized phase change as a function of propagation distance. The peaks indicate the position of the filaments along the z axis.

is clear that phase distribution exhibits a focusing behavior as a function of the propagation distance, z. This is an expected behavior for phase objects and can be used, like normal focusing in amplitude objects, to locate their position along the probe propagation axis. For the filaments (i) and (ii) in Fig. 11(a), normalized phase change distribution along the z axis is shown in Fig. 11(b). These profiles are independently created for each structure by averaging the phase change over six microns around the maximum phase change position in the transverse dimension, y. It can be clearly seen that the maximum phase change position for each filament is located at a different z position separated by ∼0.46 mm, which is in good agreement with the distances measured by the burned spot measurements. Thus, the wave-front reconstruction algorithm can indeed distinguish multiple filaments separated along the propagation direction of the probe beam when they are separated enough to avoid interaction between them.

VI. CONCLUSION

The i-HOM technique is comprehensively studied using both numerical simulations and experiments. The original wave-front retrieval algorithm and the effect of background noise are discussed by simulating phase objects and comparing the retrieved objects with the input ones. The role of the number of input in-line holograms on the convergence efficiency and accuracy of the wave-front reconstruction procedure has been discussed as well.

We have shown the power of the method in retrieving very small refractive-index changes ($\Delta n \sim 10^{-4}$) with application in laser filamentation-induced plasma strings. This estimation does not reflect the ultimate sensitivity of this technique. As our simulations show, the limit in the sensitivity of i-HOM is actually set by the amount of noise, perceived as random intensity variation, in the in-line holograms. Factors that affect the noise level in the reconstruction include the number of in-line holograms used and the actual object shape. In the case of elongated objects (such as filaments) the noise can be further reduced if we apply one-dimensional averaging, and in this case we have shown that we can increase the sensitivity to $\Delta n \sim 10^{-5}$ in the refractive-index changes. The plasma string electron-density distribution can be calculated using a simple Drude model, while the full object is revealed using Abel inversion. Finally, it is shown that i-HOM can also be successfully used to study multiple filaments with different spatial arrangements.

ACKNOWLEDGMENT

This work was supported by the European Union Marie Curie Excellence Grant "MULTIRAD" MEXT-CT-2006-042683.

[1] A. Couairon and A. Mysyrowicz, Phys. Rep. **441**, 47 (2007).
[2] B. L. Fontaine *et al.*, Phys. Plasmas **6**, 1615 (1999).
[3] G. Méchain *et al.*, Appl. Phys. B **79**, 379 (2004).
[4] S. Tzortzakis *et al.*, Phys. Rev. Lett. **86**, 5470 (2001).
[5] R. Ackermann *et al.*, Appl. Phys. B **82**, 561 (2006).
[6] J. Kasparian *et al.*, Opt. Express **16**, 5757 (2008).
[7] S. Tzortzakis *et al.*, Phys. Rev. E **64**, 057401 (2001).
[8] J. Kasparian *et al.*, Science **301**, 61 (2003).
[9] G. Méjean *et al.*, Appl. Phys. B **77**, 357 (2003).
[10] S. Tzortzakis, D. Anglos, and D. Gray, Opt. Lett. **31**, 1139 (2006).
[11] K. Stelmaszczyk *et al.*, Appl. Phys. Lett. **85**, 3977 (2004).
[12] P. Rohwetter *et al.*, Spectrochim. Acta, Part B **60**, 1025 (2005).
[13] J. D. Mills *et al.*, Appl. Phys. Lett. **81**, 196 (2002).
[14] R. R. Gattass and E. Mazur, Nat Photonics **2**, 219 (2008).
[15] D. G. Papazoglou *et al.*, Appl. Phys. A **81**, 241 (2005).
[16] S. Suntsov *et al.*, Appl. Phys. Lett. **94**, 251104 (2009).
[17] P. Panagiotopoulos *et al.*, Phys. Rev. A **82**, 061803 (2010).
[18] H. Schillinger and R. Sauerbrey, Appl. Phys. B **68**, 753 (1999).
[19] S. Tzortzakis *et al.*, Opt. Commun. **181**, 123 (2000).
[20] R. P. Fischer *et al.*, IEEE Trans. Plasma Sci. **35**, 1430 (2007).
[21] D. Abdollahpour *et al.*, Opt. Express **17**, 5052 (2009).
[22] S. Rebibo *et al.*, Laser Part. Beams **19**, 67 (2001).
[23] S. Tzortzakis *et al.*, J. Quantum Spectrosc. Radiat. Transf. **99**, 614 (2006).
[24] Q. Sun *et al.*, Opt. Lett. **30**, 320 (2005).
[25] A. Gopal, S. Minardi, and M. Tatarakis, Opt. Lett. **32**, 1238 (2007).
[26] Z. Liu *et al.*, Opt. Lett. **27**, 22 (2002).

[27] M. Centurion, Y. Pu, and D. Psaltis, J. Appl. Phys. **100**, 063104 (2006).
[28] M. Centurion *et al*., Opt. Lett. **29**, 772 (2004).
[29] D. G. Papazoglou and S. Tzortzakis, Appl. Phys. Lett. **93**, 041120 (2008).
[30] G. Rodriguez *et al*., J. Opt. Soc. Am. B **25**, 1988 (2008).
[31] T. Latychevskaia and H.-W. Fink, Phys. Rev. Lett. **98**, 233901 (2007).
[32] J. W. Goodman, *Introduction to Fourier Optics*, 2nd ed. (McGraw-Hill, New York, 1996), p. 441.
[33] G. Pedrini, W. Osten, and Y. Zhang, Opt. Lett. **30**, 833 (2005).
[34] D. Gabor, Nature (London) **161**, 777 (1948).
[35] L. Montgomery Smith, D. R. Keefer, and S. I. Sudharsanan, J. Quantum Spectrosc. Radiat. Transf. **39**, 367 (1988).
[36] F. Calegari *et al*., Phys. Rev. Lett. **100**, 123006 (2008).
[37] V. Loriot *et al*., Opt. Express **17**, 13429 (2009).
[38] S. Suntsov *et al*., Phys. Rev. A **81**, 033817 (2010).
[39] C. Rodríguez *et al*., Opt. Express **19**, 16115 (2011).
[40] V. I. Bespalov and V. I. Talanov, JETP Lett. **3**, 471 (1966).
[41] L. Bergé *et al*., Phys. Rev. Lett. **92**, 225002 (2004).
[42] G. Méchain *et al*., Phys. Rev. Lett. **93**, 035003 (2004).
[43] A. Dubietis *et al*., Opt. Lett. **29**, 1126 (2004).
[44] V. P. Kandidov *et al*., Appl. Phys. B **80**, 267 (2005).
[45] G. Fibich *et al*., Opt. Lett. **29**, 1772 (2004).